Journal of Power Sources 195 (2010) 710–719

Contents lists available at ScienceDirect

Journal of Power Sources

journal homepage: www.elsevier.com/locate/jpowsour

Structure of carbon-supported Pt–Ru nanoparticles and their electrocatalytic behavior for hydrogen oxidation reaction

Amado Velázquez, Francesc Centellas, José Antonio Garrido, Conchita Arias, Rosa María Rodríguez, Enric Brillas, Pere-Lluís Cabot*

Laboratori d'Electroquímica dels Materials i del Medi Ambient, Departament de Química Física, Universitat de Barcelona, Martí i Franquès 1-11, 08028 Barcelona, Spain

ARTICLE INFO

Article history:
Received 3 June 2009
Received in revised form 23 July 2009
Accepted 14 August 2009
Available online 22 August 2009

Keywords:
Pt–Ru nanoparticles
Electrocatalysis
Kinetic parameters
Hydrogen oxidation reaction

ABSTRACT

The electrochemical activity towards hydrogen oxidation reaction (HOR) of a high performance carbon-supported Pt–Ru electrocatalyst (HP 20 wt.% 1:1 Pt–Ru alloy on Vulcan XC-72 carbon black) has been studied using the thin-film rotating disk electrode (RDE) technique. The physical properties of the Pt–Ru nanoparticles in the electrocatalyst were previously determined by transmission electron microscopy (TEM), high resolution TEM, fast Fourier transform (FFT), electron diffraction and X-ray diffraction (XRD). The corresponding compositional and size–shape analyses indicated that nanoparticles generally presented a 3D cubo-octahedral morphology with about 26 at.% Ru in the lattice positions of the face-centred cubic structure of Pt. The kinetics for HOR was studied in a hydrogen-saturated 0.5 M H_2SO_4 solution using thin-film electrodes prepared by depositing an ink of the electrocatalyst with different Nafion contents in a one-step process on a glassy carbon electrode. A maximum electrochemically active surface area (ECSA) of 119 $m^2\,g\,Pt^{-1}$ was found for an optimum Nafion composition of the film of about 35 wt.%. The kinetic current density in the absence of mass transfer effects was 21 $mA\,cm^{-2}$. A Tafel slope of 26 $mV\,dec^{-1}$, independent of the rotation rate and Nafion content, was always obtained, evidencing that HOR behaves reversibly. The exchange current density referred to the ECSA of the Pt–Ru nanoparticles was 0.17 $mA\,cm^{-2}$, a similar value to that previously found for analogous inks containing pure Pt nanoparticles.

1. Introduction

Polymer electrolyte fuel cells (PEFCs) have been the object of extensive research in the last years because of their potential and environmentally friendly portable and transport applications [1]. The most common fuel in PEFCs apart from methanol is hydrogen, which is oxidized in the anode from reaction (1):

$$H_2 \rightarrow 2H^+ + 2e^- \quad (1)$$

Highly dispersed pure metal or alloy nanoparticles on carbon have shown good electrocatalytic performance as anodes for the above hydrogen oxidation reaction (HOR). One of the most widely used electrocatalysts is the Pt–Ru alloy, because of its large tolerance to carbon monoxide present in the hydrogen fuel coming from oil reforming. This behavior has been explained by two alternative ways: (i) through the so-called bifunctional mechanism [2], which presupposes that CO poisoning the active sites of the Pt catalyst is converted into CO_2 with participation of oxygenated species adsorbed on Ru, as expressed by reaction (2):

$$Pt–CO + Ru–OH \rightarrow Pt + Ru + CO_2 + H^+ + e^- \quad (2)$$

and/or (ii) by the electronic effect produced by alloyed Ru on CO-poisoned Pt atoms yielding a weakening of the Pt–CO bond that enhances its oxidation to CO_2 [3,4].

Several innovative syntheses of Pt–Ru nanoparticles with excellent electrocatalytic properties (particle size, dispersion, composition, etc.) for PEFCs have been proposed from microemulsion [5,6], colloidal [7,8], impregnation [9,10] and polyol [11] methods. Carbonaceous materials in the form of carbon nanotubes [12], carbon nanofibers [13], mesoporous carbon [14,15] and graphitic carbon [16] have also been recently reported as support of Pt–Ru nanoparticles. Nevertheless, partially crystalline Vulcan XC-72 carbon is currently employed as substrate of highly dispersed metal nanoparticles in commercial electrocatalysts [17].

A large number of papers have been published dealing with the structure of different unsupported and carbon-supported Pt and Pt–Ru nanoparticles and/or their electrocatalytic activity on HOR [18–40]. The kinetic parameters are usually determined by rotating disk electrode (RDE) voltammetry using an ink of the electrocatalyst deposited on a glassy carbon electrode [27]. Most inks are

* Corresponding author. Tel.: +34 93 4039236; fax: +34 93 4021231.
E-mail address: p.cabot@ub.edu (P.-L. Cabot).

0378-7753/$ – see front matter © 2009 Elsevier B.V. All rights reserved.
doi:10.1016/j.jpowsour.2009.08.039

prepared in a two-step process involving the direct deposition of the electrocatalyst on the electrode surface from aqueous slurry, followed by the coating of this layer with an appropriate amount of Nafion. The use of two-step depositions for Pt black and carbon-supported Pt electrocatalysts, for example, showed that the mass transport effects through the Nafion film on the kinetics of HOR can be avoided when its thickness is lower than 0.5 μm [20,23,27].

However, the technical electrodes are in general membrane-electrode assemblies (MEAs) prepared by deposition of the catalyst ink in one step [41–46], suggesting that the one-step deposition on glassy carbon (GC) electrodes can be viewed as a good approach to study the properties of the technical systems [40]. The suitable relative amounts of Nafion in the catalyst layers of different MEAs have been determined for carbon-supported Pt, with values in the range 30–50 wt.%, depending to a certain extent on the metal loading. The poorer performance for Nafion contents smaller than 30 wt.% has been explained by the limited proton conductivity and the incomplete wetting of catalyst by the ionomer [43,45], whereas for contents higher than 50 wt.%, the process becomes diffusion-controlled because the pore diameter decreases [42,44–46]. Maximum electrochemically active surface areas (ECSAs) for 30–40 wt.% Nafion, in agreement with these quantities, have been obtained by us using the one-step deposition technique of carbon-supported Pt catalysts on GC electrodes [40]. With Pt–Ru catalysts, the interest is mainly devoted to methanol fuel [47,48], with optimum Nafion contents in the MEAs also similar, about 25–33 wt.%, slightly increasing its performance from 15 wt.%.

In this paper, the structural and electrochemical characterization of a novel high performance (HP) commercial carbon-supported Pt–Ru electrocatalyst has been carried out. The structural properties have been determined by means of transmission electron microscopy (TEM), high resolution (HR) TEM, fast Fourier transform (FFT), electron diffraction and X-ray diffraction (XRD). As a result, the size, shape, and composition of Pt–Ru nanoparticles, as well as their dispersion over the carbon support, have been obtained. The electrochemical performance has been studied using the thin-film RDE technique with electrodes prepared by one-step deposition of electrocatalyst-Nafion inks on GC, evaluating the influence of the ionomer content in the film. The ECSAs of the different samples and the CO tolerance of the electrocatalyst have been measured by CO stripping voltammetry in 0.5 M H_2SO_4. Finally, the reversibility and kinetic parameters of HOR in the catalyst have been determined in the H_2-saturated solution. Tafel slopes, the kinetic current density in the absence of mass transfer effects related to the Nafion film thickness (j_k), and the exchange current density of HOR, have been obtained. We expect that the present results will serve as reference values to be compared with those obtained using new catalysts prepared with the same purpose.

2. Experimental

2.1. Materials and reagents

HP 20 wt.% 1:1 Pt–Ru alloy on Vulcan XC-72 carbon black (Pt–Ru/C electrocatalyst, actual analysis giving 19.9 wt.% Pt–Ru) and unsupported HP 1:1 Pt–Ru nanoparticles, used for comparison purposes, were purchased from E-Tek. The ionomer was a 5 wt.% solution of Nafion perfluorinated ion-exchange resin in a mixture of aliphatic low molecular weight alcohols (isopropanol:n-propanol in weight ratio 55:45) and water (15–25 wt.% in the mixture), supplied by Aldrich. Glassy carbon disk electrodes of 0.071 cm^2 geometric surface area were provided by Metrohm. Analytical grade 96 wt.% H_2SO_4 from Merck was used to prepare 0.5 M H_2SO_4 as the electrolyte for the electrochemical experiments. All solutions were prepared with high-purity water obtained with a Millipore Milli-Q system (resistivity > 18 MΩ cm). H_2 and Ar gases were Linde 5.0 (purity ≥ 99.999%), while CO gas was Linde 3.0 (purity ≥ 99.9%).

2.2. Physical characterization of the Pt–Ru/C electrocatalyst

The size distribution, dispersion, crystallographic phases and morphologic quantification of the Pt–Ru nanoparticles from supported electrocatalyst were analyzed by TEM and HRTEM using a JEOL JEM 2010F TEM 200 KV, which allowed obtaining the corresponding images and the electron diffraction pattern. The samples were prepared by placing a drop of a suspension obtained by ultrasonic dispersion of 0.5 mg of the Pt–Ru/C electrocatalyst in 3 ml of *n*-hexane for 10 min, over a holley-carbon copper grid and evaporating the solvent until total drying using a 40 W lamp for 15 min. TEM and HRTEM images were recorded with a Gatan MultiScan 794 CCD camera. Gatan Digital Micrograph 3.7.0 software was used for the digital treatment of images and analysis of selected areas of interest by FFT. Crystallographic data obtained from electron diffraction pattern and FFT were contrasted with CaRIne Cristallography 3.1 and PCPDFWIN 2.3 software, respectively.

XRD patterns of the supported and unsupported electrocatalyst were obtained using a PANAlytical X'Pert PRO Alpha-1 diffractometer equipped with a Cu Kα radiation (λ = 0.15406 nm). The samples were placed on a Si-Xtal support and the 2θ angle varied between 10° and 140°. Experimental diffraction patterns were modeled using a WinPLOTR 2008 sofware to fit the corresponding diffraction signals to individual peaks in order to calculate the exact value for 2θ peak angle and the width at half-height (FWHM), as well as the mean size of the nanoparticles.

2.3. Electrochemical experiments

Aqueous inks of electrocatalyst concentration between 2.5 and 10 mg ml^{-1} were prepared by sonicating different proportions of Pt–Ru/C electrocatalyst, Millipore Milli-Q water and ionomer solution for 45 min. The Nafion composition in the inks were in the range 0–80 wt.%. About 2.5–5.0 μl of each ink were then deposited with a digital micropipette, Labopette Variabel from Hirschmann or Witopet from Witeg, on the surface of the GC disk electrode and its weight was carefully measured with an accuracy of ±0.01 mg using an AG 245 Mettler-Toledo analytical balance. Afterwards, the prepared electrode was dried at room temperature for 24 h in a clean atmosphere of a dessicator. Deposited volumes of inks and electrocatalyst concentrations were chosen to obtain Pt loads on the GC surface in the range 3–40 μg cm^{-2}. Prior to the one-step deposition, the GC tip was consecutively polished with aluminum oxide pastes of 0.3 and 0.05 μm (Buehler Micropolish II deagglomerated α-alumina and γ-alumina, respectively) on a Buehler PSA-backed White Felt polishing cloth until achieving a mirror finish, being rinsed with Millipore Milli-Q water in an ultrasonic bath between polishing steps.

The compositional homogeneity and covered area of the Pt–Ru/C-Nafion ink over the GC electrode were studied by X-Ray Fluorescence (XRF) spectroscopy using a Fisher X-Ray System XDAL spectrometer, as previously described [40]. Elemental composition data obtained through XRF measurements of different areas of the inks were only used for qualitatively comparison between spectra and not for the determination of alloy composition. Inks with heterogeneous composition were ruled out for electrochemical experiments. XRF images were analyzed with Digital Micrograph 3.7.0 software to calculate the real coverage of the GC surface, which attained values over 90% in most cases.

Although in the one-step technique the catalyst is embedded in the Nafion film, we used an apparent Nafion thickness (L, in cm) in

each ink as a measure of the ionomer content (apart from the mass fraction), which was calculated from Eq. (3):

$$L = \frac{X_{Nf} w_{ink}}{\rho_{Nf} A_{GC} \theta_{GC}} \quad (3)$$

where X_{Nf} denotes the mass fraction of Nafion in the ink suspension, w_{ink} is the mass of deposited ink (g), ρ_{Nf} is the density of Nafion (1.98 g cm^{-3} [20]), A_{GC} is the geometrical area of the GC surface (cm^2) and θ_{GC} is its coverage by the Pt–Ru/C – Nafion ink measured from XRF images. Values of L between 0.03 and 5.0 μm were found for the different inks tested.

Electrochemical trials were performed with a conventional thermostated double wall three-electrode cylindrical glass cell from Metrohm of 200 ml capacity. The reference electrode was a Metrohm double junction Ag|AgCl|KCl (saturated) electrode and the counter electrode was a 3.78 cm^2 Pt bar. All potentials given in this work are referred to the RHE in the working electrolyte. All experiments were conducted at 25.0 ± 0.1 °C by water circulation through the double wall of the cell using a Julabo MP-5 thermostat. Each GC electrode covered with a Pt–Ru/C-Nafion ink was coupled to an Ecochemie Autolab RDE to be used as the working electrode. To evaluate its surface condition, characteristic cyclic voltammograms were recorded between 0.02 and 0.98 V in 0.5 M H_2SO_4 at decreasing scan rates of 100, 50 and 20 mV s^{-1} using an Ecochemie Autolab PGSTAT100 potentiostat–galvanostat with computerized control by an Autolab GPES software. After the electrode preparation, 15 cyclic voltammograms at 100 mV s^{-1} and 15 more at 50 mV s^{-1} were performed to assure the electrode cleanness. For these measurements, the electrolyte was previously deareated by sparging Ar gas for 30 min and an Ar flow was kept over it during the potential cycling. Such cyclic voltammograms were in general practically quasistationary after the second scan. Cyclic voltammograms for CO stripping under Ar atmosphere were made under similar conditions at 20 mV s^{-1}. Before beginning these trials, pure CO was bubbled through the solution for at least 15 min maintaining the electrode potential at 0.01 V to assure the complete adsorption of CO on its surface and the excess of this gas was further removed by sparging Ar for 30 min. The charge involved in CO oxidation was obtained as a function of the Pt load by the corresponding application of the GPES software, thus determining the ECSA of Pt–Ru nanoparticles in the electrocatalyst.

The HOR on the Pt–Ru/C-Nafion electrodes was studied in a H_2-saturated 0.5 M H_2SO_4 solution. This gas was previously sparged for 30 min and kept over the electrolyte during the experiments. RDE voltammograms between 0.00 and 0.40 V at a scan rate of 5 mV s^{-1} were obtained at increasing rotation rates (ω) from 400 to 3600 rpm. CO stripping voltammograms performed after these RDE experiments led to the same ECSAs as those obtained before, thus showing that there were not Pt–Ru/C-Nafion losses from the electrode during rotation.

3. Results and discussion

3.1. TEM and HRTEM analysis

TEM and HRTEM images for the Pt–Ru/C electrocatalyst are shown in Fig. 1a and b, respectively. They reveal the presence of metal nanoparticles on the surface of the Vulcan carbon black support. The examination of 115 nanoparticles showed a size distribution between 1.5 and 5.5 nm, with an average value of 3.1 nm.

The HRTEM images were also utilized to determine the two-dimensional projection areas of Pt–Ru nanoparticles to clarify their shape. These areas were also evaluated for more than 100 nanoparticles by means of a digital contrast treatment that allowed differentiating between them and the carbon support. Fig. 2 presents the measured area of the nanoparticles in front of the cor-

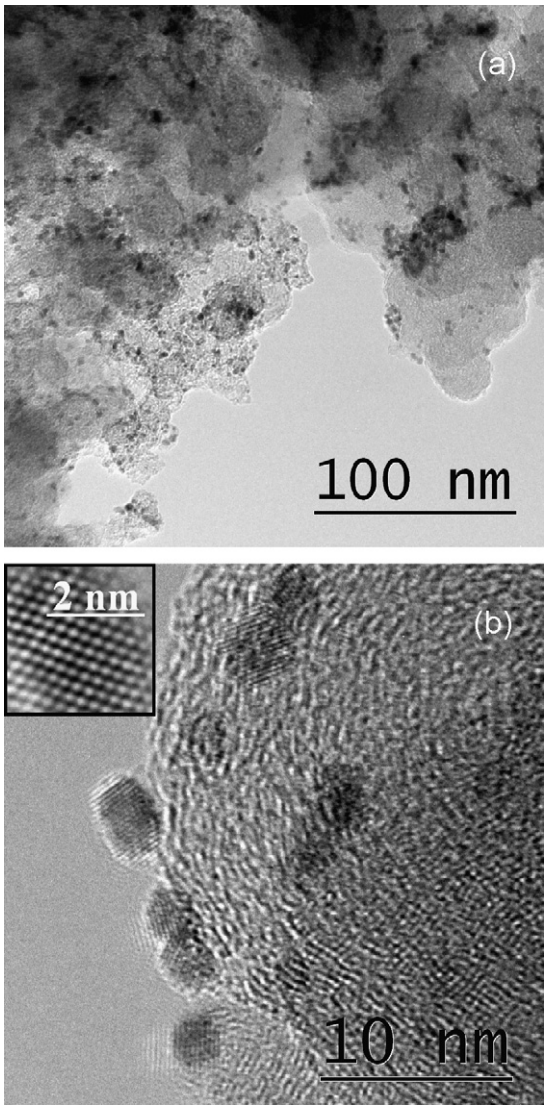

Fig. 1. (a) TEM and (b) HRTEM images of the HP 20 wt.% 1:1 Pt–Ru/C Vulcan XC-72 electrocatalyst. The inset in plot (b) shows the details of a Pt–Ru nanoparticle.

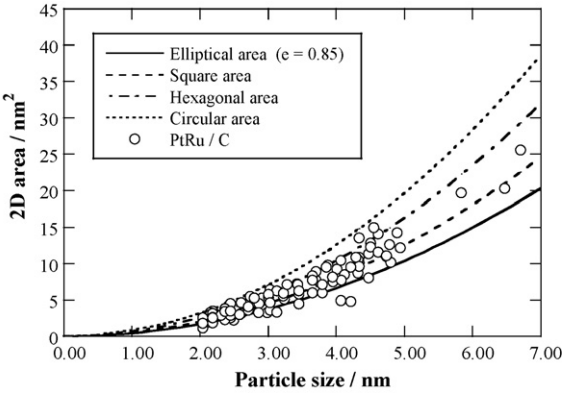

Fig. 2. Variation of the projected two-dimensional area of Pt–Ru nanoparticles with their size. The theoretical relationships for elliptical (eccentricity equal to 0.85), square, hexagonal and circular shapes are also represented (38, 34, 23, and 5% approached the square, hexagonal, elliptical and spherical form, respectively).

responding size, along with the theoretically expected relationship for elliptical, square, hexagonal and circular geometries. A predominance of projections with two-dimensional hexagonal (34%) and square (38%) geometries can be observed, which are fully compatible with a three-dimensional cubo-octahedral shape. This finding is of special interest because several works have been recently published dealing with the relation between the nanoparticle morphology and its corresponding electrocatalyst performance as fuel cell components [35,36,38]. The cubo-octahedral configuration comprises both (1 0 0) and (1 1 1) surface planes and is more stable than other morphologies such as octahedral, tetrahedral or cubic [24,28,37], then being a more useful structure for the preparation of long-term anodes for PEFCs.

Techniques coupled to TEM were employed to study the composition of the observed nanoparticles. Fig. 3a depicts the electron diffraction pattern from a global image of the Pt–Ru/C electrocatalyst. Signal 2 was related to the group of (1 1 1) planes of the face-centred cubic (FCC) structure of platinum, with an interplanar distance of $d = 0.2246$ nm. In contrast, signals 1 and 3 were tentatively assigned to certain oxides of platinum such as Pt_3O_4 ($d = 0.3949$ nm for (1 1 0) planes) and PtO_2 ($d = 0.1270$ nm for (0 1 2) planes), respectively. As shown in Fig. 3b, the FFT analyses of HRTEM images of the nanoparticles were also in agreement with the presence of PtO_x oxides, the points 1 and 2 being compatible with Pt_3O_4 ($d = 0.2454$ nm for (0 1 2) planes), 3 and 4 with PtO_2 ($d = 0.2102$ nm for (0 0 2) planes), and 5 and 6 also with PtO_2 ($d = 0.2529$ for (0 1 1) planes). However, crystalline structures of Ru or RuO_2 were not found.

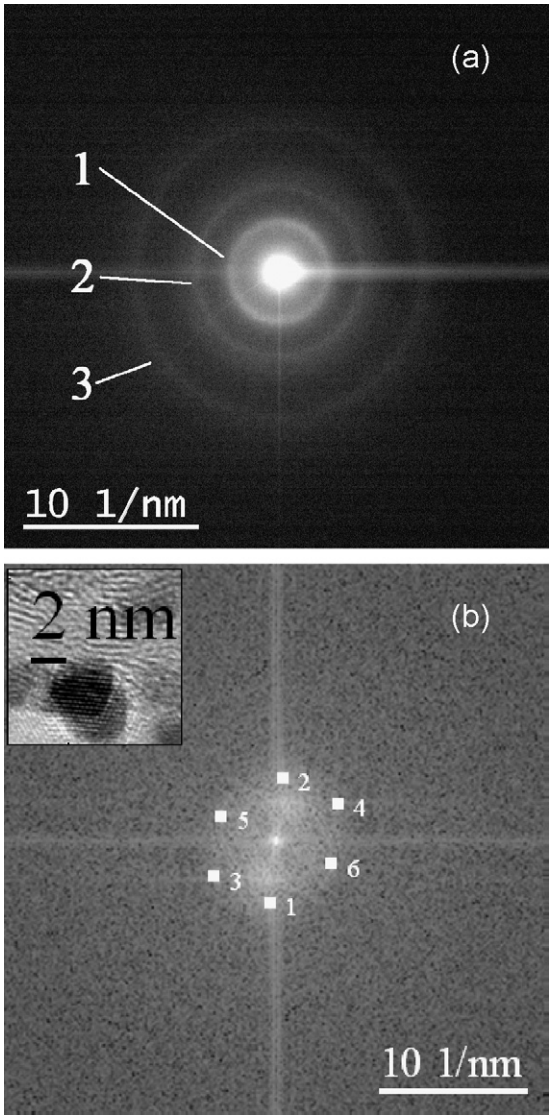

Fig. 3. (a) Electron diffraction pattern of the HP 20 wt.% 1:1 Pt–Ru/C Vulcan XC-72 electrocatalyst, showing the diffraction signals 1–3 related to Pt and PtO_x (see the text). (b) FFT analysis of the nanoparticle of the inset, the points 1–6 being compatible with PtO_x species.

The dispersion of Pt–Ru nanoparticles over the carbon support was quantitatively evaluated through statistical analysis of a selected area of a TEM image considered as representative of the electrocatalyst surface. The method is based on the evaluation of the dispersion of tracer particles in an internally circulating fluidized bed [49] and was proposed by us in our previous study on Pt nanoparticles over the same Vulcan carbon black [40]. It consists in drawing of a grid with 4×4 square cells over a sample image containing at least 50 nanoparticles, making the calculation of the average number of nanoparticles per cell (N_{cell}) and the corresponding standard deviation of the total distribution of nanoparticles in the grid (SD). The homogeneity factor (H) is then defined from Eq. (4):

$$H = \left(1 - \frac{SD}{N_{cell}}\right) \times 100 \quad (4)$$

which presupposes that the maximum homogeneity of 100% is attained when $SD = 0$. For the Pt–Ru/C electrocatalyst, $H = 62\%$ was obtained, a value similar to 57% determined previously by us for the Pt/C one [40], indicating the existence of an analogous dispersion of Pt–Ru or pure Pt nanoparticles over the Vulcan XC-72 carbon black.

3.2. XRD analysis

The X-ray diffractogram shown in Fig. 4a displays the typical peaks of the Pt FCC structure. The peak at $2\theta \approx 25^\circ$ corresponds to the (0 0 2) planes of the carbon support. For comparison, Fig. 4b depicts the XRD pattern of unsupported HP 1:1 Pt–Ru nanoparticles, which exhibits the same diffraction peaks as the supported electrocatalyst except, obviously, the carbon signal. A shift of all peaks to higher 2θ values compared to pure Pt was always found owing to the incorporation of Ru into the Pt structure, resulting in the contraction of the unit cell. For example, the (1 1 1) peak for pure Pt appears at 39.89°, whereas for Pt–Ru/C it is located at 40.22°. The lattice parameter for the Pt–Ru unit cell was $a_{Pt-Ru} = 0.3844$ nm, as determined by Eq. (5) from the corresponding interplanar distances (d_{hkl}) obtained for the different diffraction peaks of Miller index (hkl):

$$d_{hkl} = \frac{a_{Pt-Ru}}{\sqrt{h^2 + k^2 + l^2}} \quad (5)$$

The well-known Vegard's law was then applied to estimate the nanoparticle composition. It relates the lattice parameter a_{Pt-Ru} of the Pt–Ru FCC structure with the alloy degree of Ru (X_{Ru}, between 0 and 1) by Eq. (6) [31]:

$$a_{Pt-Ru} = a_{Pt} - 0.0149 X_{Ru} \quad (6)$$

where a_{Pt} is the lattice parameter of pure Pt (0.3923 nm). A value of $X_{Ru} = 0.26$ was obtained, which is significantly lower than the nominal 0.50 atomic composition. Since no signals were detected for the Ru hexagonal structure neither by electronic diffraction nor XRD, one can assume that most likely part of Ru may be either in the form of amorphous Ru or RuO_2, or incorporated into platinum oxidized phases forming mixed oxides of Pt and Ru.

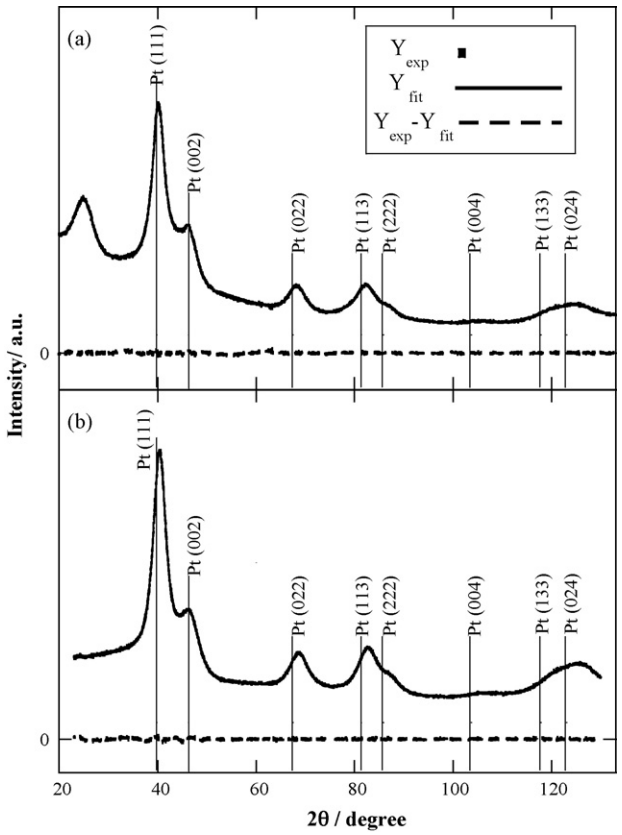

Fig. 4. Experimental and fitted XRD pattern for: (a) HP 20 wt.% 1:1 Pt–Ru/C Vulcan XC-72 electrocatalyst and (b) unsupported Pt–Ru nanoparticles.

On the other hand, the average nanoparticle size (d) was determined from the Debye–Scherrer Eq. (7) [39]:

$$d = \frac{k\lambda}{B_{2\theta}\cos\theta} \tag{7}$$

where $k = 0.9$, λ is the wavelength of the Cu Kα radiation, θ is the angle at the maximum of the peak and $B_{2\theta}$ is the width of the corresponding FWHM. A d-value of 2.6 nm was obtained for the Pt–Ru nanoparticles, slightly lower than 3.1 nm found from TEM analysis. However, the d-value thus determined by XRD is affected by the lattice strain in Pt–Ru nanoparticles, e.g., dislocations or vacancies. The Williamson–Hall analysis [50,51] was then used to correct the contribution of nanocrystal stress to the size measured. Three different approaches of the Williamson–Hall model were checked. The first approach assumes the existence of a 3D-uniform deformation or isotropic microstrain (ε) that allows calculating the corresponding nanoparticle size D from Eq. (8):

$$B_{2\theta}\cos\theta = \frac{k\lambda}{D} + 4\varepsilon\sin\theta \tag{8}$$

The other two Williamson–Hall approaches are more realistic since they include the effect of the anisotropy of the Young's modulus (E). The so-called uniform deformation stress model replaces ε in Eq. (8) by the anisotropic microstain ε_{hkl} (=σ/E_{hkl}) to give Eq. (9):

$$B_{2\theta}\cos\theta = \frac{k\lambda}{D'} + \frac{4\sigma\sin\theta}{E_{hkl}} \tag{9}$$

where D' represents the nanoparticle size, σ is the uniform deformation stress and E_{hkl} is the Young's modulus in the normal direction to the corresponding plane of Miller index (hkl). For a cubic crystal, E_{hkl} is calculated as a function of the elastic compliances s_{11}, s_{12} and s_{44} by means of Eq. (10):

$$E_{hkl} = s_{11} - (2s_{11} - 2s_{12} - s_{44})\frac{k^2l^2 + l^2h^2 + h^2k^2}{(h^2 + k^2 + l^2)^2} \tag{10}$$

To apply Eq. (10), we take the values related to the face-centred cubic (FCC) platinum, i.e., $s_{11} = 7.35\,\mathrm{TPa}^{-1}$, $s_{44} = 13.1\,\mathrm{TPa}^{-1}$ and $s_{12} = -3.08\,\mathrm{TPa}^{-1}$ [52], as acceptable elastic compliances. The third Williamson–Hall approach is the so-called uniform deformation energy density model and considers the Hooke's law to define a uniform deformation energy density or resilience (u) by Eq. (11), which can be expressed as Eq. (12) in the elastic range $\varepsilon_{hkl} = \sigma/E_{hkl}$:

$$u = \frac{\varepsilon_{hkl}^2 E_{hkl}}{2} \tag{11}$$

$$\frac{\sigma}{E_{hkl}} = \left(\frac{2u}{E_{hkl}}\right)^{1/2} \tag{12}$$

From these considerations, the Williamson–Hall equation can be written as Eq. (13):

$$B_{2\theta}\cos\theta = \frac{k\lambda}{D''} + 4\left(\frac{2u}{E_{hkl}}\right)^{1/2}\sin\theta \tag{13}$$

where D'' is the corresponding nanoparticle size.

The average sizes of the Pt–Ru nanoparticles associated with Eqs. (8), (9) and (13) for the above Williamson–Hall approaches were calculated from the plots of $B_{2\theta}\cos\theta$ with $4\sin\theta$ for the uniform deformation model (Fig. 5a), $4\sin\theta E_{hkl}^{-1}$ for the uniform deformation stress model and $2^{5/2}\sin\theta E_{hkl}^{-1/2}$ for the uniform deformation energy density model (Fig. 5b). From these linear representations, quite similar values of $D = 3.6$ nm, $D' = 3.5$ nm and $D'' = 3.5$ nm were obtained. The two latter models incorporating anisotropic factors then provide an average size which compares to 3.1 nm, the mean value measured from TEM images, indicating the existence of dislocations and others defects in the Pt–Ru nanoparticles. Note however that more precise values are expected from XRD measurements because much greater amount of particles is examined at the same time.

Finally, the specific area normalized by mass of platinum–ruthenium alloy ($S_{\mathrm{Pt-Ru}}$) or by platinum load (S_{Pt}) was determined by considering the average nanoparticle size (measured by TEM or calculated by the three Williamson–Hall approaches tested from XRD data) with the assumption of a spherical structure. The results for the specific areas obtained are collected in Table 1. Using the alloy composition data, the corresponding density of Pt–Ru nanoparticles (ρ_{alloy}) was calculated from Eq. (14):

$$\rho_{\mathrm{alloy}} = \rho_{\mathrm{Ru}}X_{\mathrm{Ru}} + \rho_{\mathrm{Pt}}(1 - X_{\mathrm{Ru}}) \tag{14}$$

Taking the fraction of Ru in the alloy ($X_{\mathrm{Ru}} = 0.26$) and the density of the pure platinum and ruthenium as $\rho_{\mathrm{Pt}} = 21.47\,\mathrm{g\,cm^{-3}}$ and $\rho_{\mathrm{Ru}} = 12.37\,\mathrm{g\,cm^{-3}}$ [53], one obtains $\rho_{\mathrm{alloy}} = 19.02\,\mathrm{g\,cm^{-3}}$.

Table 1
Morphological properties of Pt–Ru nanoparticles in the electrocatalyst, as determined by different methods.

Method	Particle size (nm)	$S_{\mathrm{Pt-Ru}}$ ($\mathrm{m^2\,g^{-1}}$)[a]	S_{Pt} ($\mathrm{m^2\,g^{-1}}$)[b]	ECSA/S_{Pt} (%)[c]
TEM	3.1	101	155	77
XRD, uniform, ε	3.6	88	133	89
XRD, uniform, σ	3.5	90	136	88
XRD, uniform, u	3.5	90	136	88

[a] Specific area normalized by mass of Pt–Ru alloy.
[b] Specific area normalized by Pt mass.
[c] Per cent ratio between the maximum ECSA (measured by CO stripping for catalyst inks with 35 ± 5 wt.% Nafion) and specific area normalized by Pt mass.

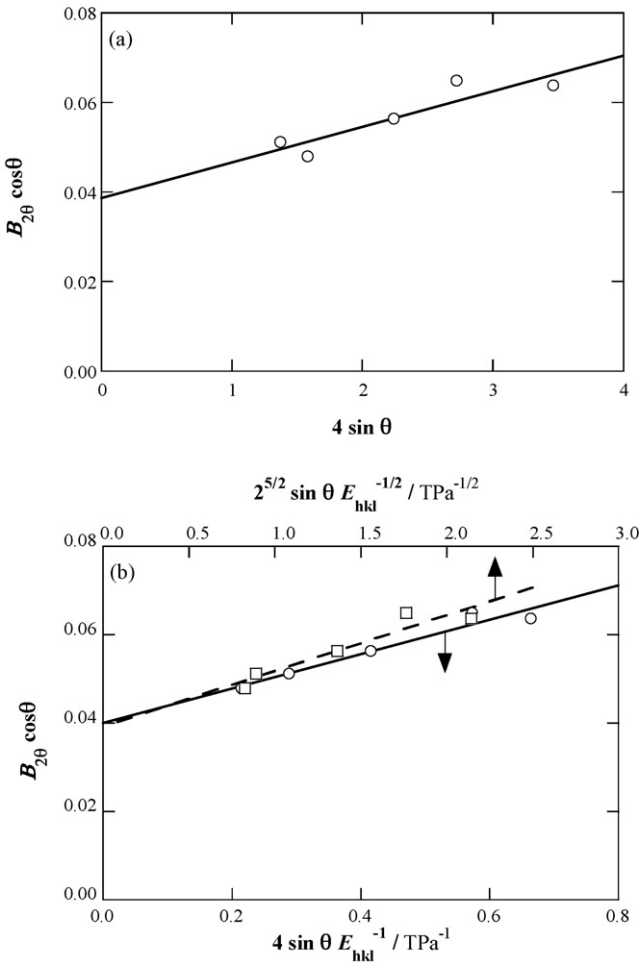

Fig. 5. Williamson–Hall plots for the HP 20 wt.% 1:1 Pt–Ru/C Vulcan XC-72 electrocatalyst assuming a: (a) uniform deformation model, (b, ○) uniform deformation stress model, and (b, □) uniform deformation energy density model.

3.3. Study of the electrocatalyst surface and CO stripping by cyclic voltammetry

Curve *a* of Fig. 6 shows a cyclic voltammogram recorded for the Pt–Ru/C-Nafion ink on GC in deareated 0.5 M H_2SO_4 solution. The upper limit of the scan was fixed at less of 1 V to prevent the loss of any Ru species by dissolution. The hydrogen monoatomic adsorption/desorption peaks appearing in the potential range of 0.01–0.20 V are very small, with charges much lower than those obtained for similar Pt/C-Nafion inks [40]. This inhibition can be accounted for by the presence of a large proportion of Ru on the nanoparticle surface. Since the exchange current density for HOR on Ru is about 0.003 A cm^{-2} [19], much smaller than the value of 0.3 A cm^{-2} for Pt [19], one can suppose, as previously suggested, that Ru does not participate in the hydrogen adsorption/desorption processes, which then becomes less favorable [33,34].

Other notable difference between the typical cyclic voltammograms for Pt–Ru/C-Nafion and Pt/C-Nafion inks on GC is the presence of a relatively high background current in the former, as can be observed in curve *a* of Fig. 6. This phenomenon is generally attributed to the discharge of water on Ru atoms to form hydroxylated species [2] by reaction (15):

$$Ru + H_2O \rightarrow Ru\text{–}OH + H^+ + e^- \quad (15)$$

The wide cathodic peak that appears at about 0.5 V can thus be assigned to the reduction of metal oxides formed in the anodic scan.

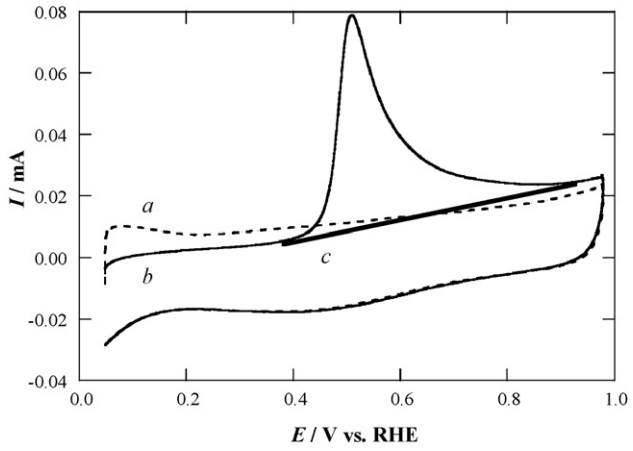

Fig. 6. Cyclic voltammograms recorded (a) in the absence of CO and (b) for the oxidation of adsorbed CO on an ink of HP 20 wt.% 1:1 Pt–Ru/C Vulcan XC-72 electrocatalyst (load of 33 μg Pt cm^{-2}) with 30 wt.% Nafion deposited on a GC disk electrode, in 0.5 M H_2SO_4 at a scan rate of 20 mV s^{-1} and 25.0 °C. In the latter case, CO was previously adsorbed at 0.01 V. The baseline *c* taken to define the CO stripping charge is also shown.

This potential is lower than 0.76 V found for pure Pt electrocatalyst [40] and it can be associated with the slower kinetics of oxide reduction. Note that the cyclic voltammogram reported in curve *a* of Fig. 6 was not altered after many repetitive scans, evidencing a large electrocatalyst stability since it is expected that the loss of Ru would produce a shift of the cathodic peak potential to a value closer to that of Pt [10].

As can be seen in curve *b* of Fig. 6, the anodic peak potential for the oxidation of CO to CO_2 is close to 0.5 V, which is much less positive than that found for Pt/C-Nafion electrodes operating under similar conditions [2–4,40], confirming the higher CO tolerance of the Pt–Ru alloy.

The charge related to the CO oxidation on different Pt loads in the electrocatalyst-Nafion ink was calculated by integrating the corresponding peak current in the cyclic voltammogram between 0.40 and 0.80 V and subtracting the baseline *c* shown in Fig. 6. Subtracting curve *a* in the CO stripping peak region does not appear adequate here because curve *b* does not retrace curve *a* near the beginning of CO stripping. CO appears to block Ru sites, thus avoiding Ru oxidation up to the beginning of CO oxidation (about 0.4 V) [2]. From these data, the ECSA of the Pt–Ru nanoparticles in the electrocatalyst was calculated assuming a charge of 420 μC cm^{-2} for the oxidation of a CO monolayer normalized by the Pt load [30]. Note that no CO oxidation was detected in a second anodic scan and that repetitive cycles allowed recovering the electrocatalytic activity for the hydrogen adsorption/desorption processes.

As can be seen in Fig. 7a, catalyst inks with Nafion contents in the range 35 ± 15 wt.% show the highest ECSAs, whereas amounts out of this range lead to smaller values. The highest value is about 15 m^2 g Pt^{-1} higher than that obtained for 70 wt.% Nafion, which is a comparable increment to that obtained with the 20 wt.% Pt/C Vulcan XC-72 catalyst studied before (increase from 60 to 73 m^2 g Pt^{-1}) [40]. The presence of a maximum in Fig. 7a can then be explained as indicated above. Fig. 7b shows the good linear correlation obtained between the charge of CO stripping and overall Pt mass deposited on the GC electrode for catalyst inks with 35 ± 5 wt.% Nafion. The slope obtained was 0.498 mC μg Pt^{-1}, which corresponds to an average ECSA of 119 m^2 g Pt^{-1}. The last column of Table 1 gives the per cent ratio between the average ECSA value of 119 m^2 g Pt^{-1} and the specific area normalized by Pt mass, either measured by TEM or calculated from the three Williamson–Hall approaches applied to the XRD data. We assume that the latter methods are more precise because XRD measurements use a much bigger amount of each

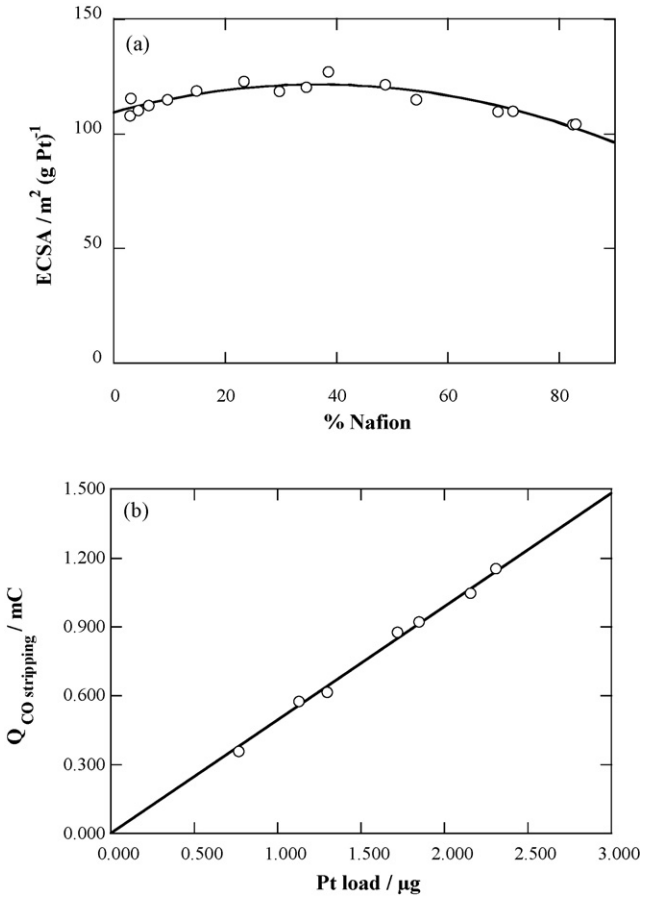

Fig. 7. (a) The dependence of the electrochemically active surface area (ECSA) of Pt–Ru, measured from CO stripping, referred to an overall Pt content of 25 ± 5 μg Pt cm^{-2}, on the Nafion content of the catalyst ink. (b) The charge of CO stripping as a function of the overall Pt load in the catalyst ink containing 35 ± 5 wt.% Nafion.

sample. The high ECSA/S_{Pt} value found in all cases indicates that a great part of the nanoparticle surface becomes electroactive. Note, however, that the real stoichiometry of the CO–Pt adsorption is still under discussion and the discrepancy between stripping and XRD measurements may be explained, at least partially, by the lack of a precise knowledge of this stoichiometry. In addition, nanoparticle surface area losses due to its contact with the carbon support and agglomeration of nanoparticles may also play a role.

3.4. Electrocatalytic performance for HOR

Thin-film RDE experiments for HOR on Pt–Ru/C-Nafion inks deposited in one step on GC disk electrodes were carried out in a H_2-saturated 0.5 M H_2SO_4 solution using different Pt loads and ionomer contents. As an example, Fig. 8 presents the hydrodynamic anodic voltammograms recorded for an ink containing 13 μg Pt cm^{-2} and 69 wt.% Nafion, which show increasing limiting current density (j_L) as ω raises from 400 to 3600 rpm. For more clarity, the corresponding cathodic waves are not plotted in this figure.

To interpret the RDE data obtained for one-step inks, a similar analytical methodology to that applied for a two-step deposition was utilized, since analogous structural model of the components in both kinds of inks can be assumed. The j_L value for HOR in a given RDE experiment can then be related by means of Eq. (16) to the following three contributions [27]: (i) the kinetic current density j_k; (ii) the boundary-layer diffusion-limiting current density (j_d),

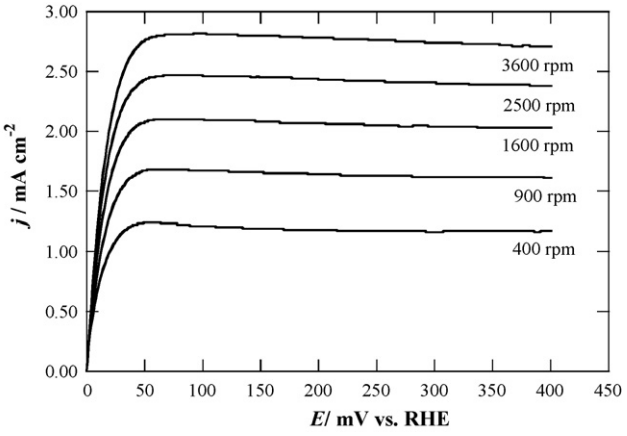

Fig. 8. Hydrodynamic voltammograms for hydrogen oxidation reactions (HOR) on an ink of HP 20 wt.% 1:1 Pt–Ru/C Vulcan XC-72 electrocatalyst (load of 13 μg Pt cm^{-2}) with 69 wt.% Nafion deposited on a GC disk electrode, in a hydrogen-saturated 0.5 M H_2SO_4 solution (after H_2 bubbling for 30 min) at different rotation rates. Scan rate 5 mV s^{-1}.

which depends on the mass transport properties in the electrolyte, and (iii) the film diffusion-limiting current density (j_f) controlled by the diffusion of H_2 through Nafion:

$$\frac{1}{j_L} = \frac{1}{j_k} + \frac{1}{j_d} + \frac{1}{j_f} \tag{16}$$

The j_d term corresponds to the Levich Eq. (17):

$$j_d = 0.62nFD^{2/3}\nu^{-1/6}C_0\omega^{1/2} = BC_0\omega^{1/2} \tag{17}$$

where n is the number of electrons involved in the oxidation reaction, F is Faraday constant (96,498 C mol^{-1}), D is the diffusion coefficient of the reactant (cm^2 s^{-1}), ν is the kinematic viscosity of the electrolyte (cm^2 s^{-1}), C_0 is the H_2 concentration in the solution (equal to its solubility, in M) and ω is the rotation speed (rpm). For 0.5 M H_2SO_4 at 25 °C, the theoretical value of BC_0 is 6.52×10^{-2} mA cm^{-2} rpm$^{-1/2}$ considering $n = 2$, $D = 3.7 \times 10^{-5}$ cm^2 s^{-1}, $\nu = 1.07 \times 10^{-2}$ cm^2 s^{-1} and $C_0 = 7.14 \times 10^{-4}$ M [19].

On the other hand, j_f can be written as:

$$j_f = \frac{nFC_fD_f}{L} \tag{18}$$

where C_f and D_f are the solubility and diffusion coefficients of H_2 in the Nafion film and L is its thickness.

Introducing Eqs. (17) and (18) into Eq. (16), one obtains:

$$\frac{1}{j_L} = \frac{1}{j_k} + \frac{1}{BC_0\omega^{1/2}} + \frac{1}{nFC_fD_fL^{-1}} \tag{19}$$

Eq. (19) expresses that j_L^{-1} is a linear function of $\omega^{-1/2}$, with a slope equal to $1/BC_0$ and a Y-axis intercept (Y_0) given by Eq. (20):

$$Y_0 = \frac{1}{j_k} + \frac{1}{nFC_fD_fL^{-1}} \tag{20}$$

This equation presupposes that Y_0^{-1} tends to j_k when the film thickness is sufficiently small. In this way, the kinetic parameters for HOR can be obtained from the corresponding plots of j_L^{-1} vs. $\omega^{-1/2}$ (Levich–Koutecky diagram) and Y_0^{-1} vs. L^{-1} or Y_0 vs. L.

For one-step deposition as in the present work, the value of L is not known, because it is assumed that the catalyst is well dispersed in Nafion. However, the j_L^{-1} vs. $\omega^{-1/2}$ plots for the different apparent Nafion thicknesses calculated from Eq. (3) were always linear, with a similar slope of $(6.5 \pm 0.5) \times 10^{-2}$ mA cm^{-2} rpm$^{-1/2}$, in excellent agreement with the theoretical value of BC_0. Fig. 9 exemplifies the characteristic Levich–Koutecky diagrams for three apparent film

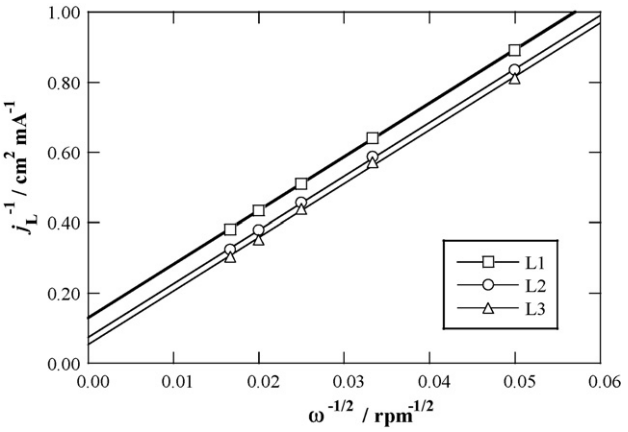

Fig. 9. Levich–Koutecky diagrams for HOR on several electrocatalyst-Nafion inks with load of 30 μg Pt cm^{-2} and apparent Nafion thicknesses of: L1 = 1.97 μm; L2 = 0.65 μm and L3 = 0.03 μm. Scan rate 5 mV s^{-1}.

thicknesses with a load of 30 μg Pt cm^{-2}. The fact that parallel linear plots with increasing j_L^{-1} as L rises are obtained confirms the influence of j_f^{-1}, which is related to the ionomer film content. Considering L in the following as the apparent film thickness obtained by Eq. (3), the relationship between Y_0^{-1} and L^{-1} for the same Pt load is depicted in Fig. 10a. Note that a similar behavior is observed when Y_0^{-1} is plotted in front of the inverse of the Nafion mass percentage in the ink, confirming the proportionality between the Nafion composition and the apparent thickness. These plots can then be suitable and quick methods for evaluating the parameter j_k. Fig. 10a also shows that Y_0^{-1} becomes practically constant, approaching j_k according to Eq. (20), when the smaller Nafion contents are used, that is, for $L < 0.2$ μm. Note that this apparent L value agrees with the critical thickness (value from which the diffusional resistance of the film is negligible) determined by Lin and Shih [32] for a Pt-black RDE from a two-step ink deposition.

By plotting Y_0 vs. L for the trials of Fig. 10a, the linear correlation of Fig. 10b is found, as predicted by Eq. (20). The Y-axis intercept is 0.047 mA^{-1} cm^2, giving j_k = 21 mA cm^{-2}. Moreover, the representation of Y_0 vs. wt.% Nafion, also shown in Fig. 10b, gives an intercept of 0.044 mA^{-1} cm^2, leading to a similar value of j_k = 23 mA cm^{-2}, which indicates that the ionomer content in wt.% is an appropriate parameter for determining the kinetic current densities. The j_k value determined for the Pt–Ru/C electrocatalyst is significantly lower, but of the same order of magnitude, than the value between 60 and 100 mA cm^{-2} reported by Gasteiger et al. [19] for smooth Pt RDEs, although it is closer to 40 mA cm^{-2} found for Schmidt et al. [23] for a two-step deposited 20 wt.% Pt/C Vulcan XC-72 electrocatalyst or 15 mA cm^{-2} obtained previously by us [40] also for 20 wt.% Pt/C Vulcan XC-72, but deposited in one step.

On the other hand, the slope of the $Y_0 - L$ plot is 4.28×10^{-2} mA^{-1} μm^{-1} cm^2, allowing estimating the $C_f D_f$ product (permeability of H_2 in the ionomer) as 1.2×10^{-5} mM cm^2 s^{-1}. Despite this value is uncertain because the real Nafion thickness that H_2 goes through is not known, it is intermediate between 4.7×10^{-6} mM cm^2 s^{-1} obtained for smooth Pt RDEs [20] and 7.8×10^{-5} mM cm^2 s^{-1} reported for a two-step deposited Pt/C-Nafion ink [23]. In addition, the difference between the $C_f D_f$ product found for one-step deposited Pt–Ru/C-Nafion ink compared to the two-step deposited Pt/C-Nafion ink can also be affected by the different structure achieved by the Nafion film depending on ink preparation, since the mass transport through the ionomer is strongly influenced by the porosity and pore size [22]. Note that the theoretical value for the permeability of H_2 in 0.5 M H_2SO_4 of $C_0D = 2.6 \times 10^{-5}$ mM cm^2 s^{-1} [19] is greater than

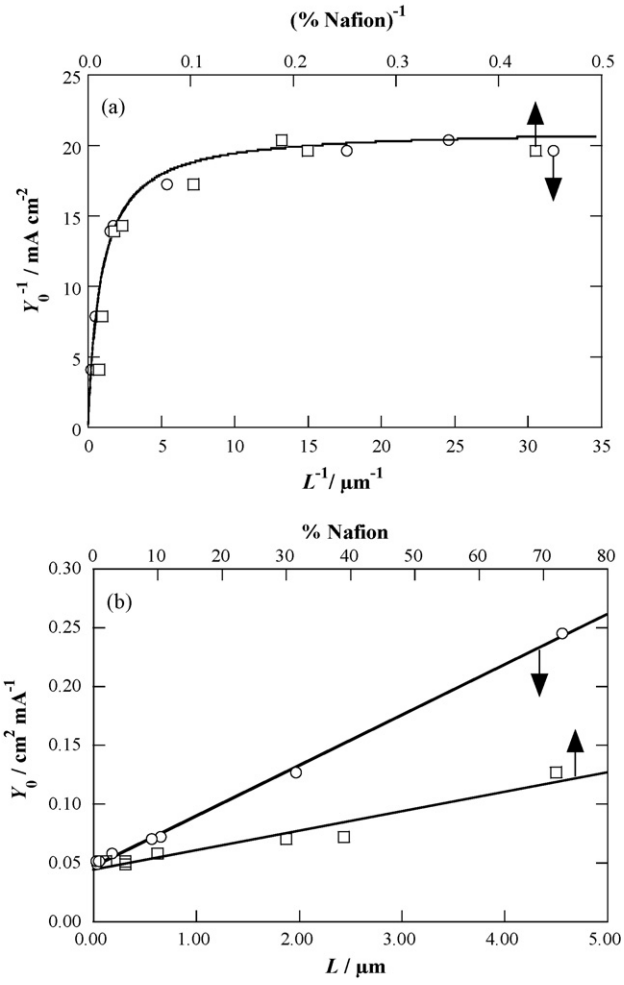

Fig. 10. (a) The inverse of Levich–Koutecky intercept (Y_0) as a function of the inverse of (○) the apparent Nafion film thickness (L) and (□) the Nafion percentage in the electrocatalyst-Nafion ink. (b) The Levich–Koutecky intercept (○) vs. the apparent Nafion film thickness and (□) vs. Nafion percentage. Load of 30 μg Pt cm^{-2} in all inks.

our estimation of $C_f D_f$, indicating a higher diffusion resistance of Nafion to H_2 transport. Although $C_f D_f$ cannot be determined with precision, the good fit of the experimental data to Eqs. (19) and (20) is indicative of the validity of the method to determine the kinetic current density.

The reversibility for HOR on the Pt–Ru/C-Nafion ink was analyzed taking into account the mass-transport corrected Tafel plots determined for the initial anodic current density growth of RDE polarization data. Under these conditions, the theoretically established Tafel equations for a reversible and irreversible electrochemical process can be expressed by Eqs. (21) and (22), respectively [21,30]:

$$E = E_1^0 - \frac{2.303RT}{nF} \log\left(\frac{I_L - I}{I_L}\right) \quad (21)$$

$$E = E_2^0 + \frac{2.303RT}{\alpha nF} \log\left(\frac{I}{I_L - I}\right) \quad (22)$$

where E_1^0 and E_2^0 are constants, I_L is the limiting current for HOR and α is the charge transfer coefficient. To do this study, current (I) values in the low overvoltage region between 0 and 21 mV were chosen. As an example, the mass transfer corrected Tafel plots for an ink with 13 μg Pt cm^{-2} and 69 wt.% Nafion at different rotation rates are presented in Fig. 11a and b assuming a reversible and irreversible reaction, respectively. In both cases, the Tafel slope is

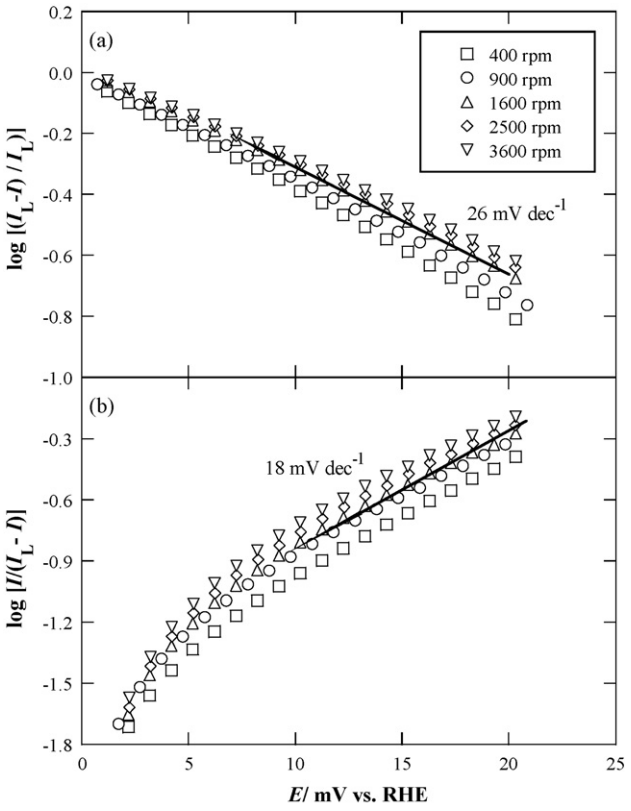

Fig. 11. Mass transfer corrected Tafel plots assuming (a) a reversible and (b) an irreversible kinetics for HOR on an ink of HP 20 wt.% 1:1 Pt–Ru/C Vulcan XC-72 electrocatalyst (load of 13 μg Pt cm^{-2}) with 69 wt.% Nafion deposited on a GC disk electrode, in 0.5 M H_2SO_4 at different RDE rotation rates. Scan rate 5 mV s^{-1}.

practically independent of rotation rate. For the reversible reaction, an average slope of 26 mV dec^{-1} is obtained, very close to the theoretical value of 29 mV dec^{-1} for a two-electron process at 298 K (see Eq. (21)). In contrast, an average slope of 18 mV dec^{-1} is determined for the irreversible reaction, very far from the theoretical value of 58 mV dec^{-1} for a two-electron process with $\alpha = 0.5$ (see Eq. (22)). No significant influence of Nafion fraction on both Tafel slopes was observed. All these results allow establishing that HOR behaves reversibly on the Pt–Ru/C-Nafion ink deposited in one step on a GC electrode.

To complete the electrochemical characterization of the Pt–Ru/C-Nafion ink, the exchange current density (j_0) for HOR was determined by using Eq. (23) [18]:

$$\frac{\Delta E}{\Delta I} = \frac{RT}{nF}\left(\frac{1}{I_0} + \frac{1}{I_L}\right) \tag{23}$$

where $\Delta E/\Delta I$ is the linear polarization slope at low overvoltage for a given ω, I_L is the corresponding limiting current and I_0 is the exchange current. The good straight line predicted by Eq. (23) between $\Delta E/\Delta I$ and I_L^{-1} at different rotation rates for an ink containing 33 μg Pt cm^{-2} and 50 wt.% Nafion is shown in Fig. 12. The slope of this plot is 13 mV, a value equal to the theoretical value of RT/nF for $n = 2$ at 298 K, confirming that HOR behaves as a two-electron reversible process on the ink tested. A $j_0 = 0.17$ mA cm^{-2} was then found by dividing the I_0 value obtained from the Y-axis intercept of the $\Delta E/\Delta I$ vs. I_L^{-1} plot by the corresponding total surface area using the ECSA value of Pt–Ru nanoparticles calculated from the above CO stripping trials. This j_0-value is very close to that determined for one- and two-step layers of Pt/C electrocatalysts synthesized with Vulcan XC-72 [29,40], indicating that HOR undergoes a similar

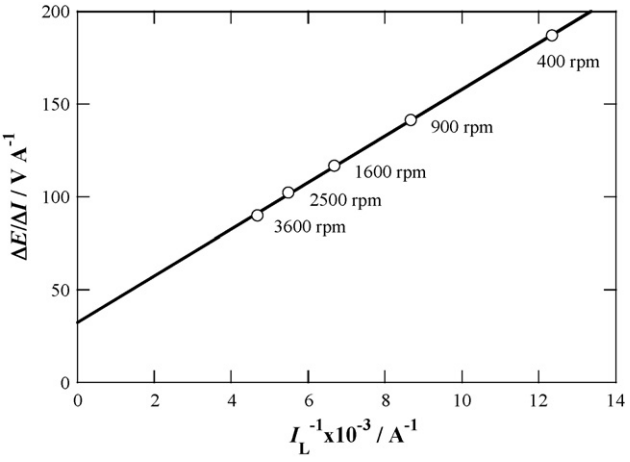

Fig. 12. Linear polarization slope ($\Delta E/\Delta I$) at different RDE rotation rates vs. the inverse of the corresponding limiting current (I_L) for HOR on an ink of HP 20 wt.% 1:1 Pt–Ru/C Vulcan XC-72 electrocatalyst (load of 33 μg Pt cm^{-2}) with 50 wt.% Nafion deposited on a GC disk electrode, in a H_2-saturated 0.5 M H_2SO_4. Scan rate 5 mV s^{-1}.

kinetic behavior using carbon-supported Pt and alloyed Pt–Ru as electrocatalysts.

4. Conclusions

TEM and XRD analysis of commercial HP 20 wt.% 1:1 Pt–Ru alloy on Vulcan XC-72 carbon black allowed determining the presence of about 26 at.% Ru in the FCC Pt lattice nanoparticles with compatible cubo-octahedral shape and with relatively good dispersion over the carbon support. An average nanoparticle size of 3.1 nm was obtained from TEM measurements, whereas a more confident value of 3.5–3.6 nm was calculated from three anisotropy-corrected Williamson–Hall models from XRD data. Cyclic voltammetry in deareated 0.5 M H_2SO_4 showed the presence of Ru on the nanoparticle surface and similar CO stripping trials indicated a great ECSA value of 119 m^2 g Pt^{-1} for the Pt–Ru nanoparticles, for optimum Nafion contents in the range 35 ± 5 wt.%, corresponding to the use of about 90% of the surface area of the nanoparticles. The HOR on novel Pt–Ru/C-Nafion inks deposited in one step on GC electrodes was studied in H_2-saturated 0.5 M H_2SO_4 by thin-layer RDE voltammetry. Taking into account the apparent ionomer film thickness calculated from Eq. (3), an excellent agreement of experimental data with analytical equations proposed for two-step deposited layers was found, as evidenced from the Levich–Koutecky diagram, as well as from the Y_0^{-1}–L^{-1} and $Y_0 - L$ plots. A kinetic current density in the absence of mass transfer effects of $j_k = 21$ mA cm^{-2} was obtained. The mass transport Tafel plots in the low overvoltage region agree with a two-electron reversible process for HOR, giving a slope of 26 mV dec^{-1}, independent of the rotation rate and the amount of Nafion deposited. The j_0-value referred to the overall area of the Pt–Ru nanoparticle was 0.17 mA cm^{-2}, which is comparable to that obtained for one- and two-step catalyst layers of similar electrocatalysts with Pt nanoparticles supported on Vulcan XC-72. Our results evidence that the electrocatalyst-Nafion inks prepared in one step are suitable to determine the kinetic parameters of HOR.

Acknowledgements

The authors thank the financial support given by the Spanish MEC (Ministerio de Educación y Ciencia) through the project NAN2004-09333-C05-03. The grant from the Fundació Pedro Pons (Universitat de Barcelona) and the FPU fellowship from Spanish MEC received by A. Velázquez to do this work are

also acknowledged. The authors also thank the SCT-UB (Serveis Científico-Tècnics de la Universitat de Barcelona) for the TEM and XRD facilities. This work is dedicated to the memory of Amado Velázquez Méndez.

References

[1] J.H. Wee, K.Y. Lee, J. Power Sources 157 (2006) 128.
[2] K. Ruth, M. Vogt, R. Zuber, Handbook of Fuel Cells—Fundamentals Technology and Applications, vol. 3, John Wiley & Sons, New York, 2003, p. 489.
[3] S. Alayoglu, A.U. Nilekar, M. Mavrikakis, B. Eichhorn, Nat. Mater. 7 (2008) 333.
[4] A.C. García, V.A. Paganin, E.A. Ticianelli, Electrochim. Acta 53 (2008) 4309.
[5] D.R.M. Godoi, J. Perez, H. Mercedes Villullas, J. Electrochem. Soc. 154 (2007) B474.
[6] X. Zhang, K.Y. Chan, Chem. Mater. 15 (2003) 451.
[7] T.J. Schmidt, M. Noeske, H.A. Gasteiger, R.J. Behm, Langmuir 13 (1997) 2591.
[8] T.J. Schmidt, M. Noeske, H.A. Gasteiger, R.J. Behm, J. Electrochem. Soc. 145 (1998) 925.
[9] D. Wang, L. Zhuang, J. Lu, J. Phys. Chem. C 111 (2007) 16416.
[10] M.S. Hyun, S.K. Kim, B. Lee, D. Peck, Y. Shul, D. Jung, Catal. Today 132 (2008) 138.
[11] S. Yan, G. Sun, J. Tian, L. Jiang, J. Qi, Q. Xin, Electrochim. Acta 52 (2006) 1692.
[12] M.C. Tsai, T.K. Yeh, C.H. Tsai, Mater. Chem. Phys. 109 (2008) 422.
[13] I.S. Park, K.W. Park, J.H. Choi, C.R. Park, Y.E. Sung, Carbon 45 (2007) 28.
[14] S.H. Liu, W.Y. Yu, C.H. Chen, A.Y. Lo, B.J. Hwang, S.H. Chien, S.B. Liu, Chem. Mater. 20 (2008) 1622.
[15] J.R.C. Salgado, J.J. Quintana, L. Calvillo, M.J. Lázaro, P.L. Cabot, I. Esparbé, E. Pastor, Phys. Chem. Chem. Phys. 10 (2008) 6796.
[16] P. Kim, J.B. Joo, W. Kim, J. Kim, I.K. Song, J. Yi, Catal. Lett. 112 (2006) 213.
[17] C. Yang, D. Wang, X. Hu, C. Dai, L. Zhang, J. Alloys Compd. 448 (2008) 109.
[18] A.J. Bard, L. Faulkner, Electrochemical Methods Fundamentals and Applications, John Wiley & Sons, New York, 1981 (Chapter 8).
[19] H.A. Gasteiger, N.M. Markovic, P.N. Ross Jr., J. Phys. Chem. 99 (1995) 8290.
[20] M. Watanabe, H. Igarashi, K. Yosioka, Electrochim. Acta 40 (1995) 329.
[21] A.S. Arico, E. Modica, E. Passalacqua, V. Antonucci, J. Appl. Electrochem. 27 (1997) 1275.
[22] J. Maruyama, M. Inaba, K. Katakura, Z. Ogumi, Z. Takehara, J. Electroanal. Chem. 447 (1998) 201.
[23] T.J. Schmidt, H.A. Gasteiger, G.D. Stäb, P.M. Urban, D.M. Kolb, R.J. Behm, J. Electrochem. Soc. 145 (1998) 2354.
[24] Z. Wang, J.M. Petrosky, T.C. Green, M.A. El-Sayed, J. Phys. Chem. B 102 (1998) 6145.
[25] A.S. Arico, P.L. Antonucci, E. Modica, V. Baglio, H. Kim, V. Antonucci, Electrochim. Acta 47 (2002) 3723.
[26] S.L. Gojkovic, T.R. Vidakovic, D.R. Durovic, Electrochim. Acta 48 (2003) 3607.
[27] T.J. Schmidt, H.A. Gasteiger, Handbook of Fuel Cells—Fundamentals Technology and Applications, vol. 2, John Wiley & Sons, New York, 2003, p. 315.
[28] A.S. Barnard, P. Zapol, J. Chem. Phys. 121 (2004) 4276.
[29] B.M. Babic, L.M. Vracar, V. Radmilovic, N.V. Krstajic, Electrochim. Acta 51 (2006) 3820.
[30] L. dos Santos, F. Colmati, E.R. Gonzalez, J. Power Sources 159 (2006) 869.
[31] Y. Le Page, C. Bock, J.R. Rodgers, J. Alloys Compd. 422 (2006) 164.
[32] R.B. Lin, S.M. Shih, J. Solid State Electrochem. 10 (2006) 243.
[33] L. Li, Y. Xing, J. Phys. Chem. C 111 (2007) 2803.
[34] Z. Liu, X.Y. Ling, B. Guo, L. Hong, J.Y. Lee, J. Power Sources 167 (2007) 272.
[35] J.S. Gullón, F.J. Vidal, A. López, E. Garnier, J.M. Feliu, A. Aldaz, Phys. Chem. Chem. Phys. 10 (2008) 3689.
[36] S. Kinge, C. Urgeghe, A. De Battisti, H. Bönnemann, Appl. Organometal. Chem. 22 (2008) 49.
[37] C. Susut, T.D. Nguyen, G.B. Chapman, Y.Y. Tong, Electrochim. Acta 53 (2008) 6135.
[38] N. Tian, Z.Y. Zhou, S.G. Sun, J. Phys. Chem. C 112 (2008) 19801.
[39] J.B. Xu, T.S. Zhao, Z.X. Liang, J. Power Sources 185 (2008) 857.
[40] I. Esparbé, E. Brillas, F. Centellas, J.A. Garrido, R.M. Rodríguez, C. Arias, P.L. Cabot, J. Power Sources 190 (2009) 201.
[41] G. Faubert, R. Cote, D. Guay, J.P. Dodelet, G. Denes, C. Poleunis, P. Bertrand, Electrochim. Acta 43 (1998) 1969.
[42] M. Uchida, Y. Fukuoka, Y. Sugawara, N. Eda, A. Ohta, J. Electrochem. Soc. 143 (1996) 2245.
[43] E. Antolini, L. Giorgi, A. Pozio, E. Passalacqua, J. Power Sources 77 (1999) 136.
[44] E. Passalacqua, F. Lufrano, G. Squadrito, A. Patti, L. Giorgi, Electrochim. Acta 46 (2001) 799.
[45] P. Gode, F. Jaouen, G. Lindbergh, A. Lundblad, G. Sundholm, Electrochim. Acta 48 (2003) 4175.
[46] G.C. Li, P.G. Pickup, J. Electrochem. Soc. 150 (2003) C745.
[47] A.S. Arico, A.K. Shukla, K.M. El-Khatib, P. Creti, V. Antonucci, J. Appl. Electrochem. 29 (1999) 671.
[48] B. Krishnamurthy, S. Deepalochani, K.S. Dhathathreyan, Fuel Cells 8 (2008) 404.
[49] X. Wei, H. Sheng, W. Tian, Int. J. Heat Mass Transf. 49 (2006) 3338.
[50] M.B. Kerber, E. Schafler, M.J. Zehetbauer, Rev. Adv. Mater. Sci. 10 (2005) 427.
[51] V. Biju, N. Sugathan, V. Vrinda, S.L. Salini, J. Mater. Sci. 43 (2008) 1175.
[52] R.F.S. Hearmon, The elastic constants of crystals and other anisotropic materials, in: K.-H. Hellwege, A.M. Hellwege (Eds.), Landolt-Börnstein New Series, vol. III/11, Springer, New York, 1979, p. 10.
[53] P. Eckerlin, H. Kandler, Structure data of elements and intermetallic phases, in: K.-H. Hellwege, A.M. Hellwege (Eds.), Landolt-Börnstein New Series, vol. III/6, Springer, New York, 1971, pp. 20–21.